ACS APPLIED MATERIALS & INTERFACES

Mutual Diffusion Occurring at the Interface between $La_{0.6}Sr_{0.4}Co_{0.8}Fe_{0.2}O_3$ Cathode and Gd-doped Ceria Electrolyte during IT-SOFC Cell Preparation

Zhi-Peng Li,*[†] Mori Toshiyuki,[†] Graeme John Auchterlonie,[‡] Jin Zou,[‡,§] and Drennan John[‡]

[†]Global Research Center for Environment and Energy Based on Nanomaterials Science, National Institute for Materials Science, Tsukuba, Ibaraki 305-0044, Japan

[‡]Centre for Microscopy and Microanalysis and [§]Division of Materials, The University of Queensland, St. Lucia, Brisbane, Queensland 4072, Australia

ABSTRACT: The microstructure and local chemistry of the interface between the screen-printed $La_{0.6}Sr_{0.4}Co_{0.8}Fe_{0.2}O_3$ (LSCF) thin film cathode and Gd-doped ceria (GDC) electrolyte substrate have been investigated. Elemental distribution analyses, by energy-dispersive X-ray spectroscopy operated in scanning transmission electron microscopy (STEM) mode, illustrate that all constituent elements in GDC and LSCF mutually diffuse across the LSCF/GDC interface, with equal diffusion length. This leads to the formation of mutual diffusion zones at the LSCF/GDC interfaces, with the resultant mixture of diffusing ions being associated with specific valence state changes, as verified by STEM electron energy loss spectroscopy analyses. Moreover, this mutual diffusion can result in microstructural changes, where superstructure formation is accompanied by enhancement of oxygen vacancy ordering at this region. Such mutual diffusion and associated microstructure evolution is considered to be detrimental to fuel cell efficiency and should be suppressed by lowering cell fabrication temperatures.

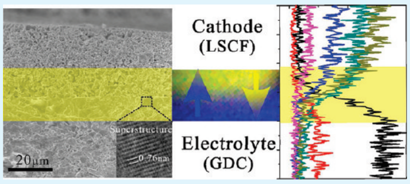

KEYWORDS: diffusion, energy-dispersive X-ray spectroscopy, electron energy loss spectroscopy, interface, microstructure, solid oxide fuel cell

1. INTRODUCTION

The past decade has witnessed significant efforts devoted to the development of intermediate temperature (500−800 °C) solid oxide fuel cells (IT-SOFCs). In comparison to conventional SOFCs currently operating around 1000 °C, IT-SOFCs have various advantages, such as shortening startup/shutdown time, reducing thermal and sealing degradation, prolonging lifetime, widening materials selection, and solving other materials problems in a cost-effective manner.[1−3] In the wake of lower operating temperatures, the electrolyte conductivity and electrode kinetics of SOFCs will be considerably reduced. To overcome these problems, a variety of solutions have been attempted, for instance, decreasing the thickness of the electrolyte to reduce ohmic loss, or choosing highly ionic conducting electrolyte materials (e.g., rare-earth-doped ceria)[4] as well as designing high-performance electrode materials (especially on the cathode side) that operate at reduced temperatures. Currently, mixed-conductor perovskite oxides $Ln_{1-x}A_xMO_{3-\delta}$ (Ln: La, Sm, Nd, Nd; A: Ca, Sr, Ba; M: Co, Fe, Ni) are widely used as the cathode materials for IT-SOFCs, to replace the traditional $La_{1-x}Sr_xMnO_{3-\delta}$ (LSM) cathode material that adequately works at 1000 °C.[5,6] Among these perovskite oxides, the $(La,Sr)(Co,Fe)O_3$ has been considered as one of the most promising candidates because of its high electronic/ionic mixed conductivities and high catalytic activities toward oxygen reduction over a wide temperature range.[7−9]

Since the chemical compatibility between electrode and electrolyte materials is a prerequisite to any further cell testing or operation, it is essential to obtain the fundamental understanding of the interaction or interdiffusion at the interfacial region. It is well-known that La-based perovskite oxides are chemically incompatible with yttria-stabilized zirconia (YSZ) electrolyte because they form insulating phases, e.g., pyrochlore $La_2Zr_2O_7$ or perovskite $SrZrO_3$.[10,11] Such oxide-ion blocking phase formation between electrode and electrolyte may lead to degradation of the electrolyte and substantially degrade cell performance. Substantial efforts were thereby put on the search for an interfacial barrier layer that inhibits the interaction or interdiffusion between the electrode and electrolyte.[12,13] A widely used material for an interlayer is rare-earth-doped ceria, e.g., Gd-doped ceria (GDC).[14−16] Also, the GDC is regarded as a potential candidate for the alternative electrolyte material of IT-SOFCs, owing to its relatively high ionic conductivity at intermediate temperatures.[17,18] It was believed that the thermochemical compatibility between $La_{1-x}Sr_xCo_{1-y}Fe_yO_3$ and ceria was sufficient under the operating conditions of IT-SOFCs.[8] Although extensive studies have been devoted to the interaction or interdiffusion between zirconia and La-based perovskite materials,[10,11] no detailed investigations have currently been performed between rare-earth-doped ceria and cathode materials. On the other hand, even though the operating temperature of IT-SOFCs is generally below 800 °C, much higher cell preparation temperatures, i.e., as high as 1000 °C or even higher, are required to fabricate mechanically stable fuel cells with

Received: May 4, 2011
Accepted: June 15, 2011
Published: June 15, 2011

high quality microstructures and porosities, as well as good adherence between different fuel cell components. Moreover, prior investigations, about the anode/electrolyte interface of the Ni/Sm-doped ceria or Ni/GDC materials systems for IT-SOFCs have illustrated that interdiffusion would take place between the anode and electrolyte and subsequently lead to interfacial layer formation, or even microstructural change.[19−22] Therefore, it is essential to explore in greater detail the cathode/electrolyte interface, to detect any possible interaction or interdiffusion, and also re-evaluate the chemical stability between the rare-earth-doped ceria and La-based perovskite materials.

In this study, the microstructure, elemental spatial distribution, interdiffusion and related evolution of valence state at the cathode/electrolyte interface have been investigated using various techniques, including scanning electron microscopy (SEM), high-resolution transmission electron microscopy (HRTEM) and scanning TEM (STEM). In the light of such detailed investigations, a fundamental understanding of the interdiffusion and associated microstructure evolution was obtained, leading to the development of high quality electrode/electrolyte interface for IT-SOFC applications.

2. EXPERIMENTAL SECTION

For electrolyte-supported half-cell fabrication, 20 at.% GDC nanopowders were used to produce a dense electrolyte substrate. The ammonium carbonate coprecipitation method was used to synthesize GDC nanopowders from respective nitrate solutions.[23,24] The resultant gel was washed, filtered and dried, then calcined at 800 °C for 2 h under flowing O_2 gas (200 mL/min) to yield the desired oxide powders. To produce a dense electrolyte, synthesized nanopowders were compacted isostatically (200 MPa) and sintered pressurelessly at 1400 °C for 6 h. For cathode material preparation, commercial $La_{0.6}Sr_{0.4}Co_{0.8}Fe_{0.2}O_3$ (LSCF) powders (Daiichi Kigenso Kagaku Kogyo Co., LTD, Japan), were initially mixed with Avicel (pore-forming agent, 5.68 wt.%), Ethyl cellulose (binder, 1.14 wt.%), and Terpineol (solvent, 36.37 wt.%). This mixture was ball milled for 12 h with a rotation rate about 1 rev/sec to obtain the homogeneous cathode slurry. The thin film cathode was fabricated by screen printing the slurry onto a GDC electrolyte substrate. Sintering of the assembled sample after screen printing occurred in a two-step method: below 500 °C, the heating rate was 2 °C/min, and increased to 5 °C/min above 500 °C, up to the target sintering temperature. The half-cell sample was then sintered at 1100 °C in air for 2 h. For a comparison of interdiffusion at different temperatures, another sample was prepared identically except for a different sintering temperature of 1400 °C, which is the same temperature at which interdiffusion occurred at the anode/electrolyte interface in a previous study.[19] Two identical sintered half-cell samples were glued together face to face for cross-sectional TEM sample preparation. After mechanical grinding and dimpling, the dimpled sample was mounted on a Mo ring for final ion milling to obtain electron-transparent thin areas.

The cathode/electrolyte interfacial morphology was initially observed using an SEM (Hitachi S-5000). More detailed microstructure studies were carried out by both HRTEM (JEOL JEM-2000EX, operated at 200 keV) and STEM (FEI Tecnai F20, operated at 200 keV). The field-emission gun (FEG) nanoprobe STEM has a Gatan image filter (GIF) which incorporates electron energy loss spectroscopy (EELS), and also has an energy-dispersive X-ray spectroscopy (EDX) detector. For STEM EDX, the FEG source was operated at 4500 V extraction voltage, with the gun lens setting of 3 in nanoprobe mode with a spot size of 3. Quantitative analyses of STEM EDX point scans, line scans and maps were performed offline using the ES Vision v4.0.172 software. For high spatial resolution, EELS was performed in STEM mode, with a reduced extraction voltage of 4200 V, gun lens setting 6 and spot size 8. Additionally, observed grains were tilted off-zone to avoid strong Bragg reflections, since strong elastic scattered peaks may interfere with the EELS spectra. Multiple scattering was also minimized by strictly following the requirement that EELS spectra were acquired at ultrathin areas with a relative thickness about 0.2−0.3 mean free path. The convergence angle and collections angle for STEM EELS were about 0.5 and 5 mrad, respectively. STEM EELS spectra were background subtracted, using a power-law function, and quantification performed using the DigitalMicrograph v1.9.3 software.

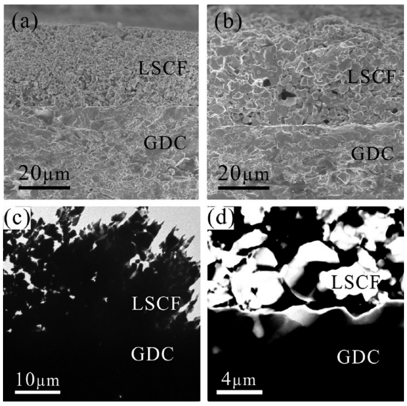

Figure 1. SEM micrographs of the interface between thin film LSCF cathode and GDC electrolyte, with the screen-printed thin film sintered at (a) 1100 and (b) 1400 °C, respectively. The cathode/electrolyte interfacial morphologies characterized by TEM are presented in (c) BF image, and (d) HAADF image, the related screen-printed thin film is sintered at 1100 °C.

3. RESULTS

3.1. Microstructure Characterization. SEM analysis, performed on a half-cell sample from a cross-sectional view, demonstrates the morphology of the cathode/electrolyte interfacial region (Figure 1). Figure 1a is the screen-printed cathode thin film sintered onto the electrolyte substrate at 1100 °C. Two distinct regions, corresponding to LSCF cathode and GDC electrolyte, can be clearly recognized. The screen-printed thin film is porous with uniform homogeneous grain size distribution. A good adherence between the porous cathode thin film with respect to the dense electrolyte substrate can be seen from Figure 1a. The higher sintering temperature (i.e., 1400 °C) for the screen-printed thin film results in larger grain formation, as shown in Figure 1b. Moreover, the higher temperature sintered thin film has good porosity and is well adhered onto the dense substrate (Figure 1b). From SEM observations, all powders at both the cathode and electrolyte sites have sintered together with high adhesion. Figure 1c is a typical TEM bright field (BF) image, which presents the similar interfacial morphology of the porous thin film adhered onto the dense substrate. Figure 1d is a STEM HAADF image, formed due to differences in the atomic number of the elements present and their thickness (the thickness of porous thin film can be easily reduced during ion-milling process when compared to the dense substrate), the cathode/electrolyte interface can be clearly recognized.

More detailed microstructures are observed by HRTEM. Figure 2a is a typical region observed around the cathode/electrolyte interface. Figure 2b is the related diffractogram of the region A (marked by the solid line square) in Figure 2a. This indicates that the GDC grain, with pure fluorite structure, is observed along the [112] zone axis. Interestingly, at the nearby region, different microstructures can be observed. Figure 2c is the diffractogram of the specific region B (marked by dashed line square) in Figure 2a. Note that besides the diffraction spots arising from fluorite structure, extra periodic diffraction spots appear, implying that superstructure formation occurs on the basis of the ceria lattice. By carefully indexing these diffraction patterns, the suggestion is that this superstructure is due to long-range order along the ceria ⟨220⟩ direction, with a periodicity four times larger than the related intervals of fluorite {220} lattice. The interval of this long-range ordered structure (~ 0.76 nm) can be measured directly from the HRTEM image as shown in Figure 2a, and it is about four times that of the ceria {220} lattice spacing ($d_{\text{ceria}\{220\}} = 0.191$ nm), which is consistent with the result interpreted from the diffractogram in Figure 2c. Figure 2d is another typical region observed at the GDC grain around the cathode/electrolyte interface, from which similar superstructure (with periodic lattice spacing of 0.76 nm) can be clearly seen. These spacings can also be confirmed from the corresponding diffractogram shown in Figure 2e. Similar superstructure can also be observed at the grain boundary region around the cathode/electrolyte interface, as shown in the Figure 2f. It needs to emphasize that this superstructure is only observed at the cathode/electrolyte interface. Different from the preparation process of anode/electrolyte half-cell sample, where H_2 gas treatment was used to reduce NiO to Ni, the cathode/electrolyte sample has never been treated in H_2. Therefore, the superstructure observed at the cathode/electrolyte sample should not be attributed to the reduction of Ce^{4+} to Ce^{3+}, as previously reported.[21,22]

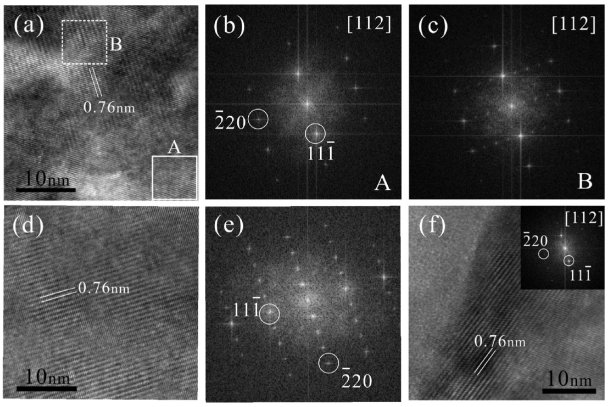

Figure 2. (a) HRTEM image of detailed microstructures of GDC observed around the cathode/electrolyte interface, the corresponding diffractograms of the specific regions marked in a are shown in b and c, respectively. (d) Another typical area around the interfacial region with similar superstructure formation, the corresponding diffractogram is shown in e. (f) Grain boundary region with similar superstructure formation, the related diffractogram is shown as an inset.

3.2. Mutual Diffusion at the Cathode/Electrolyte Interface. To address the aforementioned issue, that superstructures are mainly formed at the cathode/electrolyte interface, we further investigated the two-dimensional elemental distribution at the interfacial region. Figure 3a is a STEM BF image of two edge-on grains observed at the cathode/electrolyte interface. The elemental compositions were qualitatively determined by STEM EDX mapping. From the respective elemental maps, Ce, Gd, La, Sr, Co, and Fe as represented from Figures 3b−g, as well as the reconstruction map (Figure 3h, combing all the elemental maps from Figures 3b−g), the GDC grain of the electrolyte and LSCF grain of the cathode can be clearly recognized. Note that the sharp grain boundary, which is represented in STEM BF image (Figure 3a), disappears in all the elemental maps. Instead, there is a contrast gradient around the grain boundary, implying the difference of elemental concentration at the boundary region. Consequently, quantitative STEM EDX line scan was performed across the grain boundary, denoted by the yellow dash line in Figure 3a. The corresponding concentration profile is shown in Figure 3i. As seen from the profile in Figure 3i, both LSCF and GDC grain interiors have homogeneous chemical compositions. However, around the grain boundary, there is an overlap among different elements, demonstrating the existence of elemental exchange between the materials in contact. According to the concentration profile (Figure 3i), it can be interpreted that La has transported from the grain of LSCF to GDC. This is easy to understand, since La cation has already been verified as a mobile element.[6] Interestingly, not only does La migrate, but also other elements can diffuse into their nearby grains. Figure 3i illustrates that all the cations in both LSCF and GDC can mutually diffuse into the adjacent grain across the related grain boundary. Furthermore, all the migrating elements have similar diffusion lengths, resulting in a mutual diffusion zone (about 200 nm wide) formed at the interface.

More STEM EDX measurements in the cathode/electrolyte interfacial region confirmed the mutual diffusion zone formation between contacting LSCF and GDC grains. For comparison, quantitative measurements were conducted upon samples sintered at both 1100 and 1400 °C. Figure 4a is the concentration profile of STEM EDX line scan acquired from another 1100 °C sintered sample. Similar to the result shown in Figure 3i, all

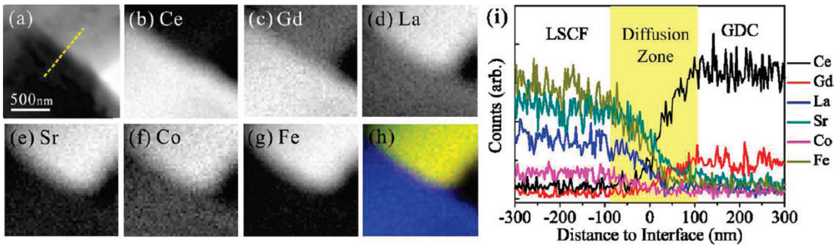

Figure 3. (a) STEM BF image of two contacting grains observed at the cathode/electrolyte interface. (b−g) Elemental maps acquired at the region shown in a by STEM EDX mapping, and (h) reconstructed image combining all the elemental maps. The concentration profile of STEM EDX line scan conducted across the grain boundary, denoted by the dashed line in a.

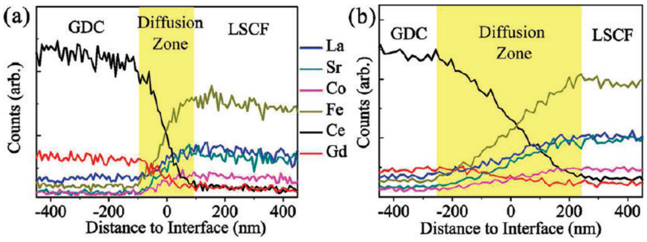

Figure 4. Concentration profiles of STEM EDX line scans conducted across the cathode/electrolyte interfaces, the corresponding screen-printed thin films were sintered at (a) 1100 and (b) 1400 °C, respectively.

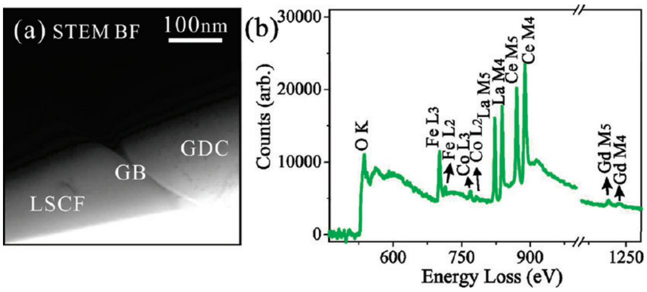

Figure 5. (a) STEM BF image of two contacting LSCF and GDC grains observed at the cathode/electrolyte interface. (b) STEM EELS acquired at this region, with the energy loss ranging from 500 to 1300 eV.

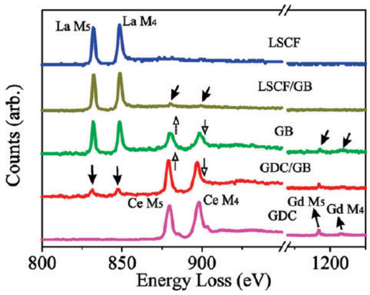

Figure 6. STEM EELS results acquired at different sampling positions, namely, the LSCF grain interior (LSCF), the LSCF grain interior near the grain boundary (LSCF/GB), the grain boundary (GB), the GDC grain interior (GDC), and the GDC grain interior near the grain boundary (GDC/GB), at the region shown in Figure 5a.

Table 1. Different Element Concentrations Exptrapolated from STEM EELS Data

	La (at %)	Ce (at %)	Gd (at %)
GDC	0 ± 2.6	72.54 ± 8.3	27.46 ± 6.7
GDC/GB	12.06 ± 1.3	56.56 ± 5.7	31.38 ± 5.5
GB	38.01 ± 2.5	34.43 ± 6.5	27.56 ± 6.3
LSCF/GB	86.78 ± 9.1	8.74 ± 7.7	4.48 ± 4.1
LSCF	100 ± 9.4	0 ± 2.9	0 ± 3.1

constituent elements in LSCF and GDC grains were transported from one phase to the other, accompanied with similar diffusion lengths and resulting in the formation of a mutual diffusion zone (with average width of 200 nm). As can be expected, increasing the sintering temperature will significantly enhance the migration of cations and lead to a wider mutual diffusion zone (with average width of 500 nm) formation at the LSCF/GDC interface, as demonstrated in Figure 4b. This hence reveals that mutual diffusion is a temperature-dependent behavior.

3.3. Valence State and Element Concentration Analyses by STEM EELS. As mentioned above, the mutual diffusion zone, with the mixture of diffusing cations, will form in terms of mutual diffusion which occurred at the LSCF/GDC grain boundaries around the cathode/electrolyte interface. It is hence essential to investigate the valence state of each cation in this mutual diffusion zone. Figure 5a is a representative STEM BF image of two contacting grains observed at the cathode/electrolyte interface. The compositions of each grain were determined by using STEM EDX point scans, as denoted in the figure. A STEM EELS spectrum was initially acquired at the grain boundary region with a dispersive energy of 1 eV per channel, to obtain the overall spectra from energy loss 500 to 1300 eV, the corresponding result is shown in Figure 5b. All the peaks can be indexed as O, Fe, Co, La, Ce, and Gd, as marked in the spectrum, which reveals the existence of a mutual diffusion zone with mixed diffusing ions. Repeated STEM EELS measurements were subsequently performed at different specific locations, assigned as the LSCF grain interior (denoted as LSCF hereafter), the GDC grain interior (GDC), the related grain boundary (GB), the LSCF area near grain boundary (LSCF/GB), and the GDC area near grain boundary (GDC/GB), respectively. The corresponding STEM EELS results are presented in Figure 6. At grain interiors, only homogeneous compositions can be detected by STEM EELS. For instance, in the spectrum of GDC grain interior (the pink line in Figure 6), only typical Ce-$M_{4,5}$ peaks (with the ionization threshold energy at 883 eV) and Gd-$M_{4,5}$ peaks (1185 eV) were observed. However, note the spectrum acquired at the GDC/GB (the red line in Figure 6), weak extra peaks (denoted by two solid arrows) other than those arising from Ce and Gd appeared, which were indexed as La-$M_{4,5}$ (832 eV). Similarly, extra peaks (i.e., Ce-$M_{4,5}$, marked by two solid arrows) were also be observed at the LSCF/GB interface (the brown line in Figure 6). At the grain boundary, all the peaks of La, Ce, and Gd can be clearly seen, as presented by the green line in Figure 6. Moreover, STEM EELS can provide not only the qualitative elemental information, but also the quantitative data about concentrations of different compositions. The quantified results of the STEM EELS spectra presented in Figure 6 are listed in Table 1. In Table 1, a comparison of relative changes of elemental concentration is presented for different locations as marked in Figure 4a. It should be noticed that the La concentration decreases from the grain interior to grain boundary but does not fade away at the grain boundary. Instead, the concentration of La gradually dissolves into the GDC grain. Similar phenomenon can be observed for the Ce and Gd concentration gradients. This concentration variation of different elements around the grain boundary is in agreement with the aforementioned STEM EDX line scan analyses. Therefore, the STEM EELS results presented in Figure 6 and Table 1, not only reveal the existence of mixed ions in LSCF/GDC grain boundary, but also indirectly identify the mutual diffusion occurring at this region.

It is worth noting that, in Figure 6, not only are extra peaks observed, but also the evolution of spectral peaks of individual element occurs around the grain boundary region (highlighted by open arrows). More detailed STEM EELS spectra are shown in

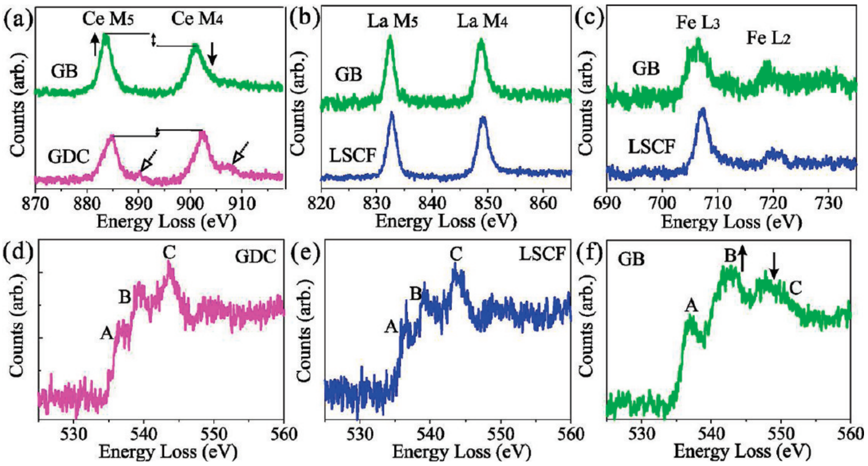

Figure 7. STEM EELS results comparing the spectra of (a) Ce $M_{4,5}$ peaks, (b) La $M_{4,5}$ peaks, (c) Fe $L_{2,3}$ peaks acquired at related grain interiors and the grain boundary. (d−f) are STEM EELS spectra of oxygen K-edge peaks acquired at grain interiors of GDC, LSCF and the grain boundary between them.

Figure 7. Figure 7a compares the Ce-$M_{4,5}$ acquired at the grain boundary and interior separately. The typical features Ce-$M_{4,5}$, such as the twin peaks accompanied with related shoulders of each peak (marked by two open arrows in Figure 7a), are clearly seen in the spectrum acquired from the GDC grain interior (the pink line in Figure 7a). This indicates that the predominant Ce cations are in the tetravalent state. However, the spectrum acquired at the grain boundary shows different peak features. The M_5 peak is enhanced and the intensity is stronger than M_4 peak. The intensity ratio of Ce M_5 to M_4 peaks (I_5/I_4) changed remarkably, from ~0.87 (I_5/I_4 of the pink spectrum in Figure 7a) to ~1.30 (I_5/I_4 of the green spectrum in Figure 7a), accompanied by disappearance of the two shoulders. This fine structure change implies that Ce^{3+} is the predominant valence state at the grain boundary region. However, such fine structural changes in EELS peaks were not observed for La $M_{4,5}$ (Figure 7b) and Fe $L_{2,3}$ (Figure 7c) peaks in our investigations. Not only were cations valence states determined, but the oxygen spectra were also acquired in this study. Figure 7d−f shows oxygen K-edge adsorption peaks acquired at the grain interiors of both GDC and LSCF, and the grain boundary between them (the same area shown in Figure 4a). It should be noted that typical oxygen A, B, C peaks can be clearly seen and are similar in both GDC and LSCF grain interiors. However, the fine structure of the oxygen K-edge acquired at the grain boundary is different, with a pronounced enhancement of the B peak (highlighted by arrows in Figure 7f). This fine structure of oxygen K edges can be used as the fingerprint to determine the evolution of the level of oxygen vacancy ordering.[19,20,24] Therefore, the appearance of a pronounced oxygen K-edge B peak can be interpreted in terms of the enhancement of local oxygen vacancy ordering at the grain boundary.

4. DISCUSSION

According to all examined specimens, no secondary phases were detected, and both of the crystallographic structures of the cathode and electrolyte were preserved. It was known that solid-state transport at the interface can also result in diffusional porosity, as a result of the so-called Kirkendall effect.[25] Nevertheless, because of the limited mutual diffusion length, i.e., less than 500 nm for all investigated samples, the significant microstructural changes such as that arising from the Kirkendall effect have not been detected. To some extent, this implies the chemical compatibility of LSCF and GDC at such temperature ranges. However, it should be pointed out that even though there is no secondary phase formation, or diffusional porosity occurred at the LSCF/GDC interface, it does not mean that the interaction or interdiffusion between the LSCF and GDC grains can be neglected as previously reported.[8,26]

The mutual diffusion, with an average mutual diffusion length of ~200 nm at 1100 °C and ~500 nm at 1400 °C, was validated at the cathode/electrolyte interface. In previous reports,[14,15,27] it was considered that the diffusion barrier layer GDC should be dense to efficiently inhibit the interdiffusion between the electrode and electrolyte, and consequently maximize the electrical/ionic conductivity. Nevertheless, our investigations demonstrate that mutual diffusion still occurs even in dense GDC, through the contacting area between LSCF and GDC grains. All the cations in LSCF and GDC can mutually migrate and substitute for each other, independent of the material, that is, whether it is dense or porous. Moreover, as opposed to previous reports, where only the La caion diffused into ceria due to the mobility of the cation from the perovskite sublattice A,[6] nor the high diffusion rates of the transition metals (e.g., Co and Fe) and Sr from the perovskite to ceria occurred, without rare-earth elements diffusion,[28] the present study revealed that all cations migrate and mutually diffuse into each other with an equal diffusion length. Owing to the significant difference of the ionic radius of the diffusing ions, substitutional diffusion is believed to be the predominant mechanism. Also, because of the variation in the radius of the substituted cations, this may act as a trigger for the valence state evolution of diffusing ions by compensation through substitution mismatch. As verified by the STEM EELS, trivalent Ce is the predominant valence state only within the mutual diffusion zone. This infers that the reduction of cerium (from Ce^{4+} to Ce^{3+}) may take place as a consequence of the cerium diffusion and substitution of cations in the sublattice of the perovskite structure.[26] However, it is unknown for the point that the substitution of Ce for cations into either A or B, or both sublattices of perovskite structure. This issue can be further clarified with more precise structural techniques, such as neutron powder diffraction or extended X-ray adsorption fine structure.

Note that such mutual diffusion may not only result in the valence state change of the diffusing cations ions but may also lead to microstructural evolution at the interface. As represented in Figure 2, substitution of cations with different ionic radii (compared to host Ce and Gd) causes lattice mismatch accumulated by the substitutional diffusion that will be released by rearrangement of the cations, e.g., in a long-range ordered structure. This situation may be revealed by the enhancement of oxygen vacancy ordering at the mutual diffusion zone, which is in accordance with the appearance of superstructure formation at the LSCF/GDC grain boundary. It can be anticipated that the changes in composition, as a result of elemental mutual diffusion between the cathode and electrolyte, may lead to changes in not only the microstructures but also the electrical properties of the materials. For instance, it was reported that the substitution of Co for Ga in LSGM electrolyte would correspondingly increase the ionic conductivity.[29] On the other hand, because of the highly ordered ion lattice, the superstructure formed at the LSCF/GDC grain boundary (in other words, the cathode/electrolyte interface), may inhibit the free movement of cations or oxygen vacancies around this region. As a consequence, this highly ordered structure formation at the interface may be considered the blocking structure, inhibiting the movement of mobile charge carriers and lowers the ionic conductivity accordingly. This may provide the possible reason for the recent investigation that, the GDC barrier layer actually has considerably negative influence on the performance of LSM/YSZ composite electrodes.[30]

Substantial studies have illustrated that the addition of an ionic conductor (e.g., GDC) to the mixed electronic/ionic conductor (e.g., LSCF) may improve cathodic performance in IT-SOFCs.[7] Particularly, 3d metals, in practice, do not form solid solution with ceria, because of the large differences in ionic radii.[6] Also, it was believed that the insertion of lanthanum into fluorite ceria could be negligible due to the good chemical stability between La-based perovskite and ceria.[28] However, this study elucidates that, even though GDC and LSCF have good chemical stability, mutual diffusion can still take place at their interface and lead to microstructural change. Such microstructure evolution is detrimental for high-quality cell operation, and this mutual diffusion should be suppressed. Note, that in all samples, the nanopowders and the screen-printed thin films are all well-sintered, which can provide good conductivity pathways. Meanwhile, the well-sintered ceramics and the good adherence at the interface also provide pathways for interdiffusion among constituent elements.

According to the comparison of mutual diffusion length of samples sintered at 1100 and 1400 °C, this reveals that such mutual diffusion is temperature dependent. It is thereby desirable to lower the sintering temperature during fuel cell fabrication, in order to minimize the mutual diffusion or formation of other possible solid solutions between the two materials at the cathode/electrolyte interface.

5. CONCLUSIONS

The interface of the LSCF cathode screen-printed on GDC electrolyte has been systematically studied in this present work. The morphology of the LSCF/GDC interface has been characterized by both SEM and TEM, which demonstrated that the porous thin film LSCF cathode is well-adhered onto the dense GDC electrolyte substrate. In contrast to previous reports,[8,26,28] STEM EDX in this study demonstrates that mutual diffusion may take place at the interface between the LSCF cathode and GDC electrolyte. Not only does Ce and Gd diffuse from the electrolyte to the LSCF cathode, but also La, Sr, Co, and Fe diffuse from the cathode and penetrate into GDC. Particularly, all diffusing cations have equal diffusion length, indicating that mutual diffusion is dominated by substitution mechanism. Moreover, STEM EELS analyses verified that the mutual diffusion may lead to a valence state change among diffusing cations. The typical phenomenon is the reduction of Ce^{4+} to Ce^{3+} to compensate for the radius variation during substitution. The pronounced fine structure changes of the oxygen K-edge revealed the enhancement of oxygen vacancy ordering at the mutual diffusion zone, verified by STEM EELS. This can be attributed to long-range order within the structures, i.e., the superstructure formation at the LSCF/GDC contacting regions. Mutual diffusion should be suppressed/avoided by all means, because of the highly ordered superstructure formation and related negative effect upon fuel cell performance. According to the comparison of mutual diffusion length at different sintering temperatures, this type of mutual diffusion is dependent upon sintering temperature. It must be emphasized that such mutual diffusion occurred before fuel cell operation. Therefore, the fuel cell fabrication or stack construction should be carried out at the lowest possible temperature, to minimize mutual diffusion at the cathode/electrolyte interface.

AUTHOR INFORMATION

Corresponding Author

*Tel.: +81-29-8513354 ext. 8544. Fax: +81-29-8604712. E-mail: LI.Zhipeng@nims.go.jp.

ACKNOWLEDGMENT

The present work is financially supported by the Grant-in-Aid for Scientific Research 22310053 for Ministry of Education, Culture, Sports, and Technology (MEXT), Japan. We also thank the Global Research Center for Environment and Energy based on Nanomaterials Science (GREEN), National Institute for Materials Science, Japan, for partial financial support. Z.P.Li thanks Mr. Suzuki Akira, and Dr. Zhimin Li for sample preparation assistance.

REFERENCES

(1) Minh, N. Q. *J. Am. Ceram. Soc.* **1993**, *76*, 563.

(2) Steele, B. C. H.; Heinzel, A. *Nature* **2001**, *414*, 345.

(3) Jacobson, A. J. *Chem. Mater.* **2010**, *22*, 660.

(4) Steele, B. C. H. *Solid State Ionics* **2000**, *129*, 95.

(5) Qiu, L.; Ichikawa, T.; Hirano, A.; Imanishi, N.; Takeda, Y. *Solid State Ionics* **2003**, *158*, 55.

(6) Zajac, W.; Swierczek, K.; Molenda, J. *J. Power Sources* **2007**, *173*, 675.

(7) Roosmalen, J. A. M.; Cordfunke, E. H. P. *Solid State Ionics* **1992**, *52*, 303.

(8) Murray, E. P.; Sever, M. J.; Barnett, S. A. *Solid State Ionics* **2002**, *148*, 27.

(9) Miguel, A. L. B; Kilner, J. A.; Skinner, S. J. *Chem. Mater.* **2010**, *22*, 1134.

(10) Stochniol, G.; Sysakis, E.; Naoumidis, A. *J. Am. Ceram. Soc.* **1995**, *78*, 929.

(11) Yokokawa, H. *Annu. Rev. Mater. Res.* **2003**, *33*, 581.

(12) Tsoga, A.; Gupta, A.; Naoumidis, A.; Nikolopoulos, P. *Acta Mater.* **2000**, *48*, 4709.

(13) Brugnoni, C.; Ducati, U.; Chemelli, C.; Scagliotti, M.; Chiodelli, G. *Solid State Ionics* **1995**, *76*, 183.

(14) Mai, A.; Haanappel, V. A. C.; Tietz, F.; Stover, D. *Solid State Ionics* **2006**, *177*, 2103.

(15) Knibbe, R.; Hjelm, J.; Menon, M.; Pryds, N.; Sogaard, M.; Wang, H. J.; Neufeld, K. *J. Am. Ceram. Soc.* **2010**, *93*, 2877.

(16) Kungas, R.; Bidrawn, F.; Vohs, J. M.; Gorte, R. J. *Electrochem. Solid-State Lett.* **2010**, *8*, B87.

(17) Waller, D.; Lane, J. A.; Kilner, J. A.; Steele, B. C. H. *Solid State Ionics* **1996**, *86*, 767.

(18) Zhang, T. S.; Ma, J.; Luo, L. H.; Chan, S. H. *J. Alloys Compd.* **2006**, *422*, 46.

(19) Li, Z. P.; Mori, T.; Auchterlonie, G. J.; Guo, Y. N.; Zou, J.; Drennan, J.; Miyayam, M. *J. Phys. Chem. C* **2011**, *115*, 6877.

(20) Li, Z. P.; Mori, T.; Auchterlonie, G. J.; Zou, J.; Drennan, J. *Phys. Chem. Chem. Phys.* **2011**, *13*, 9685.

(21) Ou, D. R.; Mori, T.; Ye, F.; Miyayama, M.; Nakayama, S.; Zou, J.; Auchterlonie, G. J.; Drennan, J. *J. Electrochem. Soc.* **2009**, *156*, B825.

(22) Ye, F.; Mori, T.; Ou, D. R.; Zou, J.; Drennan, J.; Nakayama, S.; Miyayama, M. *Solid State Ionics* **2010**, *181*, 646.

(23) Mori, T.; Wang, Y.; Drennan, J.; Auchterlonie, G. J.; Li, J. G.; Ikegami, T. *Solid State Ionics* **2004**, *175*, 641.

(24) Li, Z. P.; Mori, T.; Auchterlonie, G. J.; Zou, J.; Drennan, J. *Appl. Phys. Lett.* **2011**, *98*, 093104.

(25) Paul, A.; Vandal, M. J. H.; Kodentsov, A. A.; Vanloo, F. J. J. *Acta Mater.* **2004**, *52*, 623.

(26) Konysheva, E.; Irvine, J. T. S.; Besmehn, A. *Solid State Ionics* **2009**, *180*, 778.

(27) Uchida, H.; Arisaka, S.; Watanabe, M. *Solid State Ionics* **2000**, *135*, 347.

(28) Sakai, N.; Kishimoto, H.; Yamaji, K.; Horita, T.; Brito, M. E.; Yokokawa, H. *J. Electrochem. Soc.* **2007**, *154*, B1331.

(29) Ullmann, H.; Trofimenko, N.; Naoumidis, A.; Stover, D. *J. Eur. Ceram. Soc.* **1999**, *19*, 791.

(30) Hansen, K. K.; Menon, M.; Knudsen, J.; Bonanos, N.; Mogensen, M. *J. Electrochem. Soc.* **2010**, *157*, B309.